

# Interfacial settling mode and tail dynamics of spherical-particle motion through immiscible fluids interfaces

Zhiqiang Chen<sup>a</sup>, Moran Wang Ph.D<sup>a,\*</sup>, Shiyi Chen<sup>b,c</sup>

<sup>a</sup> Department of Engineering Mechanics and CNMM, Tsinghua University, Beijing 100084, China

<sup>b</sup> State Laboratory of Turbulence and Complex Systems, Peking University, Beijing 100871, China

<sup>c</sup> Southern University Science and Technology, Shenzhen 518055, Guangdong, China

## HIGHLIGHTS

- A LBM-DEM coupling model is developed for particle moving through immiscible fluid interface.
- The numerical results revealed that Reynolds number is not the key parameter governing the interfacial settling mode.
- There exists a critical  $Ca$  characterizing the transition from film drainage mode to tailing mode.
- A higher  $Ca$  results in a larger final tail length and a pinch-off position closer to the middle of tail.

## ARTICLE INFO

### Article history:

Received 16 June 2020

Received in revised form 10 August 2020

Accepted 29 August 2020

Available online 3 September 2020

### Keywords:

Interfacial settling  
Interface deformation  
Tail dynamics  
Tailing mode  
LBM-DEM

## ABSTRACT

Particles motion through a fluid–fluid interface is of both academic and industrial interests, yet, underlying mechanisms have not been fully understood. In this work, a two-phase LBM-DEM coupling model is developed to systematically explore the behavior of a particle moving through an immiscible fluid–fluid interface under different physical conditions. After validations, the current model reproduces two typical interface deformation modes, film drainage mode and tailing mode, successfully. The numerical results reveal that Reynolds number ( $Re = RV/\nu$ ) is not the key parameter governing the interfacial settling mode, because a smaller  $Re$  from larger upper fluid viscosity ( $\nu$ ) is conducive to the occurrence of tailing mode, but a smaller  $Re$  from smaller particle radius ( $R$ ) or smaller settling velocity ( $V$ ) makes film drainage mode take place more easily. The regime map in Capillary number ( $Ca$ ) and viscosity ratio ( $\lambda$ ) diagram shows that there exists a critical  $Ca$  characterizing the transition from film drainage mode to tailing mode, which is nearly independent of the viscosity ratio ( $\lambda$ ) yet increases with the reduced particle size ( $R$ ). The tail dynamics analysis shows that a higher  $Ca$  results in a larger final tail length and a pinch-off position closer to the middle of tail.

© 2020 Elsevier Ltd. All rights reserved.

## 1. Introduction

The particle transport through a fluid–fluid interface is of great interest in many natural processes and industrial applications (Geller et al., 1986; Kundakovic and Vunjak-Novakovic, 1995; Pierson and Magnaudet, 2018a; Su et al., 2019; Sutherland et al., 2018; Zhao et al., 2020). In nature, for instance, particle settlement in the ocean is commonly observed where the fluid–fluid interface exists owing to discontinuous density or viscosity (Ardekani et al., 2017; Burns and Chemel, 2015; Lee et al., 2019; Panah et al., 2017). For industrial applications the coating process and the liquid–liquid extraction are two typical ones. In the coating process, a solid sub-

strate crosses the fluid–fluid interface and then its surface is coated with a thin film (Tsai et al., 2011). To extract two liquids mixing with each other, the droplets need break through the interface and eventually coalesce to form its bulk phase (Geller et al., 1986). Comprehensive understanding of such complex problems needs to start from the transport mechanism of one single particle through a fluid–fluid interface.

During the past few decades, quite a few efforts have been made to explore the mechanisms governing different modes with which the particle crosses the deformable fluid–fluid interface (Dietrich et al., 2011; Geller et al., 1986; Jones and Wilson, 1978; Manga and Stone, 1995; Pierson and Magnaudet, 2018a). Pioneering studies mainly focus on the film drainage mode (hereinafter called film drainage) (Geller et al., 1986; Jeffreys and Davies, 1971), where a fluid film exists between particle and interface,

\* Corresponding author.

E-mail address: [mrwang@tsinghua.edu.cn](mailto:mrwang@tsinghua.edu.cn) (M. Wang).

which is gradually drained until the particle contacts the interface. An early review about the theoretical analysis of film drainage was given in (Jeffreys and Davies, 1971). Jones and Wilson (1978) analyzed the film drainage process with the matched asymptotic expansion method which was later improved in (Smith and Vandeven, 1984) by considering the influence from film gravity. Experimental explorations about film drainage were reported in (Hartland, 1969; Princen, 1963; Shah et al., 1972). Geller et al. (1986) numerically showed that film drainage only corresponded to the situation where the particle crossed the interface with the slowest velocity or under quasi-steady conditions (Pierson and Magnaudet, 2018a). Otherwise, other modes, such as the splash mode (Truscott et al., 2014) or the tailing mode (Maru et al., 1971) might appear. Splash mode takes place when the particle impacts the interface with a sufficiently large velocity (Pierson and Magnaudet, 2018a). A recent review about the splash mode was given in (Truscott et al., 2014), where the particle geometry, material properties, fluid properties and other impact parameters were systematically considered.

When a particle passes through the fluid-fluid interface with a moderate velocity, tailing mode is observed. In this mode, a long slender tail of the upper fluid is entrained into the lower one even though the particle has not contacted with the interface (Geller et al., 1986; Maru et al., 1971; Pierson and Magnaudet, 2018a). The tail eventually pinches off either at its middle part or close to the particle surface. Early experimental identifications of tailing mode were given in (Maru et al., 1971). After that, systematic explorations of this configuration have been seldom reported, even though it commonly occurs in the two-phase fluid system with comparable densities (Pierson and Magnaudet, 2018a). A numerical study on tailing mode was given in (Geller et al., 1986), which only considered the interface deformation before the pinch-off process. De Folter et al. (2010) experimentally studied the passage of a rigid sphere through a fluid-fluid interface in a colloid-polymer mixture, and obtained different transport modes by changing the particle size. Dietrich et al. (2011) investigated the effects from the particle size and the interfacial tension on the tail length. Very recently, Pierson and Magnaudet (2018a) have qualitatively analyzed tailing mode by various dimensionless parameters and considered a large range of viscosity ratio between the two fluid components.

Experiments can efficiently describe the interface deformation in tailing mode, but provide little information to understand the underlying physics. Thus, further explorations are needed to obtain new insights. For example, various dimensionless parameters were used to characterize the settling mode, including Bond number ( $Bo$ ), Capillary number ( $Ca$ ), Archimedes number ( $Ar$ ) and Reynolds number ( $Re$ ) (Pierson and Magnaudet, 2018a). However, the systematic study on the key dimensionless parameters governing the transition from film drainage to tailing mode is still not enough. In addition, the tail dynamics (such as the velocity distribution in the tail) is crucial in determining the final tail length and the rupture position, but is not easily obtained from the experiments (Dietrich et al., 2011). Thus, the purpose of this work is to numerically figure out the proper dimensionless parameters determining the interfacial deformation mode and explore the involved mechanisms based on tail dynamics.

The direct simulation of particle suspension in a two-phase fluid system is always a big challenge owing to the need to accurately capture the interface deformation and its interactions with the solid particles. During the past few decades, the lattice Boltzmann method (LBM) has been further developed to simulate two or three phase fluid flow (Milan et al., 2020; Song et al., 2013; Wei et al., 2018; Xie et al., 2018; Xie et al., 2016). Recently, it has been coupled with discrete element method (DEM) to study the fluid-solid coupling process (Chen et al., 2015; Chen and Wang,

2017; Chen et al., 2016; Chen et al., 2018), which provides a promising way to directly simulate the passage of a solid particle through the fluid-fluid interface. The existing LBM-DEM coupling models only focused on two fluid components with comparable kinematic viscosity (Chen et al., 2015). However, the kinematic viscosity ratio between the two fluid components is an important parameter, whose range may cover 4–5 orders of magnitude in various situations (Pierson and Magnaudet, 2018a). We overcome this limitation with a new two-phase LBM-DEM coupling model, which can deal with high viscosity ratios. A comprehensive description and validation of the new model is provided in Section 2. We therefore apply this method to explore the transport process of a rigid sphere moving through the fluid-fluid interface.

## 2. Numerical methods and validations

In this part, a new multiphase fluid-solid coupling model is introduced first, including the lattice Boltzmann method for two-phase fluids and the LBM-DEM coupling scheme for fluid-solid interaction. The numerical model is validated by some classic benchmark cases.

### 2.1. Numerical models

#### 2.1.1. Lattice Boltzmann method for multiphase fluids

The Shan-Chen two-phase multicomponent lattice Boltzmann model is a pseudo-potential model (Shan and Chen, 1993; 1994), where two distribution functions are introduced to represent two immiscible components. For the component  $k$  ( $k = 1, 2$ ), the distribution function is given by

$$f_i^k(\mathbf{x} + \mathbf{e}_i \Delta t, t + \Delta t) - f_i^k(\mathbf{x}, t + \Delta t) = \Omega_{coll}^k + \mathbf{F}, \quad (1)$$

where  $\Omega_{coll}^k$  is the collision term and  $\mathbf{F}$  is the external force term. In the single-relaxation-time (SRT) formulation

$$\Omega_{coll}^k = \frac{f_i^{eq,k}(\mathbf{x}, t) - f_i^k(\mathbf{x}, t)}{\tau_k}, \quad (2)$$

where  $\tau_k$  is the dimensionless relaxation time related to the fluid kinematic viscosity

$$v_k = \frac{(\tau_k - 1/2)\delta_x^2}{3\delta_t}. \quad (3)$$

In Eq. (3),  $\delta_t$  is the time step, and  $\delta_x$  is the lattice size. In the two-dimensional-ninth-speed model (D2Q9), the discrete velocities are

$$\mathbf{e}_i = \begin{cases} 0, & i = 0 \\ c(\cos[(i-1)\pi/4], \sin[(i-1)\pi/4]), & i = 1, 3, 5, 7 \\ \sqrt{2}c(\cos[(i-1)\pi/4], \sin[(i-1)\pi/4]), & i = 2, 4, 6, 8 \end{cases}, \quad (4)$$

where  $c = \delta_x/\delta_t$  is the lattice speed. The equilibrium distribution for the D2Q9 model is given as

$$f_i^{eq}(\rho, \mathbf{u}) = \rho \omega_i \left[ 1 + \frac{\mathbf{e}_i \cdot \mathbf{u}}{3c^2} + \frac{9(\mathbf{e}_i \cdot \mathbf{u})^2}{2c^4} - \frac{3\mathbf{u} \cdot \mathbf{u}}{2c^2} \right], \quad (5)$$

where the weighting factors are

$$\omega_i \begin{cases} 4/9, & i = 0 \\ 1/9, & i = 1, 3, 5, 7 \\ 1/36, & i = 2, 4, 6, 8 \end{cases}. \quad (6)$$

After evolution, the macroscopic density and velocity are calculated by

$$\rho_k = \sum_i f_i^k, \quad (7)$$

and

$$\mathbf{u}_k = \frac{\sum_i f_i^k \mathbf{e}_i}{\rho_k} \quad (8)$$

For a two-phase fluid system, the total velocity is calculated by

$$\mathbf{u} = \frac{\sum_k \rho_k \mathbf{u}_k}{\sum_k \rho_k} \quad (9)$$

In the previous two-phase LBM-DEM coupling models (Chen et al., 2015; Gunther et al., 2013), the original Shan-Chen scheme (Shan and Chen, 1993; 1994) was used, where the viscosity ratio between two components had to be smaller than 5 for obtaining a stable result (Porter et al., 2012). In order to overcome this limitation, a new two-phase LBM model in (Porter et al., 2012) is applied for the current LBM-DEM coupling framework. Compared with the previous ones, two modifications are made here. First, an explicit force (EF) scheme is applied to consider the external force in Eq. (1). Second, the multiple-relaxation-time (MRT) formulation is used.

In the explicit forcing (EF) scheme, the external force term in Eq. (1) is the average value of  $f_i^{F,k}(\mathbf{x} + \mathbf{e}_i \Delta t, t + \Delta t)$  and  $f_i^{F,k}(\mathbf{x}, t)$ ,

$$\begin{aligned} & f_i^k(\mathbf{x} + \mathbf{e}_i \Delta t, t + \Delta t) - f_i^k(\mathbf{x}, t + \Delta t) \\ &= \Omega_{coll}^k + \frac{\Delta t}{2} \left[ f_i^{F,k}(\mathbf{x} + \mathbf{e}_i \Delta t, t + \Delta t) + f_i^{F,k}(\mathbf{x}, t) \right]. \end{aligned} \quad (10)$$

The force term in Eq. (10) is defined by (He et al., 1998)

$$f_i^{F,k} = 3 \frac{\mathbf{F}_k \cdot (\mathbf{e}_i - \mathbf{u}^{eq})}{\rho_k c^2} f_i^{eq,k}, \quad (11)$$

where  $\mathbf{F}_k$  is the interactive force between two components to prevent them from mixing with each other and is calculated via the following equation

$$\mathbf{F}_k = -\rho_k(\mathbf{x}) \sum_{\mathbf{e}_i} \sum_k G_{kk}^-(\mathbf{x}, \mathbf{x} + \mathbf{e}_i) \rho_k^-(\mathbf{x} + \mathbf{e}_i), \quad (12)$$

where  $G_{kk}^-(\mathbf{x}, \mathbf{x} + \mathbf{e}_i) = G_{kk}^-(\mathbf{x}, \mathbf{x} + \mathbf{e}_i)$ , and  $\rho_k$  is the density of the  $k$ -th component. In the D2Q9 model,  $G_{kk}^-(\mathbf{x}, \mathbf{x} + \mathbf{e}_i)$  is written as

$$G_{kk}^-(\mathbf{x}, \mathbf{x} + \mathbf{e}_i) = \begin{cases} g_{kk}^-, & \text{if } |e_i| = \delta_x \\ g_{kk}^-/4, & \text{if } |e_i| = \sqrt{2}\delta_x, \\ 0, & \text{otherwise} \end{cases} \quad (13)$$

where  $g_{kk}^-$  is a positive value whose magnitude determines the value of the surface tension in the two-phase fluid system.

The multiple-relaxation-time (MRT) formulation is used in the current model, where the collision term is redefined as

$$\Omega_{coll}^k = \mathbf{T}^{-1} \Lambda \mathbf{T} \left[ f_i^{eq,k}(\mathbf{x}, t) - f_i^k(\mathbf{x}, t) \right], \quad (14)$$

where  $\mathbf{T}$  is the transformation matrix given in Appendix A, and  $\Lambda$  is the diagonal matrix of the relaxation parameters

$$\Lambda = \text{diag} \left( s_c^k, s_e^k, s_v^k, s_c^k, s_q^k, s_c^k, s_q^k, s_v^k, s_v^k \right), \quad (15)$$

where  $s_e^k, s_v^k, s_q^k$  are the free parameters, and  $s_v^k = 1/\tau_k$ . More details about the current two-phase Shan-Chen scheme have been reported in (Porter et al., 2012).

In the current model, wetting properties are controlled by introducing an interactive force between the fluid and the solid phases, which is intuitively and easily implemented. If the attractive force between fluid A and the solid is larger than that between fluid B and solid, fluid A and B will be the wetting and non-wetting phase, respectively. A virtual density for the solid nodes is introduced to calculate the solid/fluid interactive force (by Eq. (12)) and given by

$$\rho_{k(solid)}(\mathbf{x}) = \rho_{k(solid)}^{ave}(\mathbf{x}) + \Delta s_k, \quad (16)$$

where  $\rho_{k(solid)}(\mathbf{x})$  is the virtual density of  $k$ -th component at the solid node  $\mathbf{x}$ , and  $\rho_{k(solid)}^{ave}(\mathbf{x})$  is the average density of the surrounding  $k$ -th component around the solid node at the position  $\mathbf{x}$  (Chen et al., 2015). The parameter  $\Delta s_k$  ( $\Delta s_{wetting} = -\Delta s_{non-wetting}$ ) in Eq. (16) is the virtual fluid density, which is a positive value for the wetting phase and affects the interactive forces on the wetting and non-wetting component. By changing the value of  $\Delta s_k$ , different contact angles can be achieved.  $\Delta s = 0$  means a neutral-wetting case.

### 2.1.2. LBM-DEM coupling scheme for fluid-solid interaction

In order to couple the two-phase fluid flow and the solid motion, two aspects should be considered. First, a no-slip boundary condition should be satisfied on the solid surface, which can be achieved by treating similarly as in the single-phase fluid for each individual component. Second, the capillary force applied at the fluid-fluid-solid contact point should be calculated accurately.

#### A. Midway bounce-back boundary condition

The midway bounce-back scheme is used to ensure the no-slip boundary on the solid surface, which is widely used for the particle suspension simulation (Aidun et al., 1998; Ladd, 1994a, 1994b). In this scheme, the solid boundary lies in the midpoint of each boundary link connecting the solid and the fluid nodes. For the fluid nodes near the solid ones, the midway bounce-back boundary condition is applied by

$$f_z^k(\mathbf{x}_f, t + \Delta t) = \tilde{f}_z^k(\mathbf{x}_f, t) - 6\omega_z \rho \frac{\mathbf{e}_z \cdot \mathbf{u}_w}{c^2}, \quad (17)$$

where  $\mathbf{u}_w$  is the velocity on the midpoint of the boundary link,  $\mathbf{x}_f$  is the fluid node next to the solid one,  $\mathbf{e}_z$  is the direction from the fluid to the solid node,  $\tilde{f}$  is the opposite direction, and  $\tilde{f}$  is the distribution function after collision.

#### B. Hydrodynamic force calculation

In a two-phase fluid-solid coupled system, the hydrodynamic force imposed on the solid particle includes two parts. The first one is calculated by the classic momentum exchange method,

$$\mathbf{F}_h^k = - \left[ f_{\tilde{z}}^k(\mathbf{x}_f, t) \mathbf{e}_{\tilde{z}} - \tilde{f}_z^k(\mathbf{x}_f, t) \mathbf{e}_z \right]. \quad (18)$$

When the solid particle covers or uncovers the fluid nodes, the impulse forces should be added and are written as (Aidun et al., 1998)

$$\mathbf{F}_{cover}^k(\mathbf{x}) = \sum_{k=1}^2 \sum_{i=1}^8 f_i^k(\mathbf{x}) \mathbf{e}_i, \quad (19)$$

$$\mathbf{F}_{uncover}^k(\mathbf{x}) = - \sum_{k=1}^2 \sum_{i=1}^8 f_i^k(\mathbf{x}) \mathbf{e}_i. \quad (20)$$

When the particle suspends at the interface of two components, the capillary force applied at the fluid-fluid-solid point should be considered. It is calculated by the sum of the fluid-solid interactive force acting on the whole solid nodes. More details about how to couple two-phase LBM and DEM can be found in (Chen et al., 2015).

## 2.2. Validations

Before discussing the particle motion through a fluid-fluid interface, a series of benchmarks have been performed to validate

the current two-phase LBM-DEM coupling model. First, the accuracy of the two-phase LBM part is verified, and then the two-phase LBM-DEM coupling model is validated.

2.2.1. Validations for two-phase LBM

To validate the two-phase LBM part, two benchmark cases have been considered. The physical model of the first one is in Fig. 1a, where a spherical bubble (red) is located at the center of another fluid (blue). For a 2D bubble at an equilibrium state, the pressure difference inside and outside of the bubble is determined by the Laplace's law

$$P_{in} - P_{out} = \frac{\sigma}{R}, \tag{21}$$

where  $\sigma$  is the surface tension,  $R$  is the radius of the bubble. In the current simulation, the computational domain is a square with a  $200 \times 200$  grid, and a periodic boundary is applied at boundaries. The densities of two fluid components are the same, and the kinematic viscosity (normalized by  $\delta_x^2/\delta_t$  in this work) is listed in Table 1. In the LBM model,  $g_{12} = g_{21} = 0.38$  is used to prevent the two components from mixing with each other. We consider two schemes (SRT and MRT) and four cases are simulated where the bubble diameters equal to 41, 60, 70 and 78, respectively.

Fig. 1b shows the linear curve of fitting the simulation results and the slope corresponds to the surface tension. It indicates that both the SRT and MRT results obey the Laplace's law, while the MRT scheme can capture a high viscosity ratio up to 500.

In the second case, a 2D multilayer flow is simulated to verify the accuracy of the two-phase LBM algorithm under a dynamic condition. As shown in Fig. 2a, three parallel layers of fluids are bounded by two infinite plates. The thickness for the fluid layers is equal to 50, 100 and 50, respectively. Two fluids, A (red) and B (blue), are considered, whose properties are the same except for the kinematic viscosity. The kinematic viscosity ratios between fluid B and fluid A equal to 0.01, 0.1, 10 and 100, respectively. A constant body force is applied in both fluid A and B to drive the whole system. No-slip boundary conditions are implemented on the top and bottom walls, and periodic boundary conditions are used for inlet and outlet. The simulation parameters are listed in Table 2. When the steady state is reached, the fluid velocity profiles can be compared with the analytical solutions (see Appendix B). Fig. 2b shows very good agreements between our numerical results and the analytical solutions.

Table 1  
LBM parameters in the first benchmark.

SRT	Group 1	$v_{red} = v_{blue} = 0.033$	$\tau_{red} = \tau_{blue} = 0.6$
	Group 2	$v_{red} = v_{blue} = 0.167$	$\tau_{red} = \tau_{blue} = 1$
	Group 3	$v_{red} = v_{blue} = 0.333$	$\tau_{red} = \tau_{blue} = 1.5$
MRT	Group 1	$v_{red} = 0.00667, v_{blue} = 3.33$	$\tau_{red} = 0.51, \tau_{blue} = 10.5$

2.2.2. Validations for two-phase LBM-DEM coupling

The capillary force at the three-phase contact point is an important factor that may influence the particle motion passing through the fluid-fluid interface. For a given two-phase fluid-solid system, the static contact angle is uniquely determined by the capillary force at the three-phase contact point. Based on this point, we calculate the contact angle using two different methods for a given two-phase fluid-solid system.

The schematic of the first method is shown in Fig. 3a, where a droplet attached on a fixed flat wall is directly simulated using the two-phase LBM. At the steady state, the contact angle ( $\alpha$ ) can be calculated by the following equations

$$R = \frac{a_0}{2} + \frac{b_0^2}{8a_0}, \tag{22}$$

$$\tan(\alpha) = \frac{b_0}{2(R - a_0)}, \tag{23}$$

where  $R$  is the drop radius, and the meaning of  $a_0$  and  $b_0$  is shown in Fig. 3. A  $200 \times 200$  lattice system is used, and the density and viscosity of the two fluids are identical respectively ( $v_{red} = v_{blue} = 0.00667$ ). Different values (0.02, 0.04, 0.06, 0.08, 0.1, 0.12, and 0.14) of the parameter  $\Delta s_{red}$  are considered to achieve the different contact angles.

The other way to calculate the contact angle is demonstrated in Fig. 3b, where a solid spherical particle is suspended in the two-phase fluid system with the center at the fluid-fluid interface initially. Owing to the capillary force at the three-phase contact point, the particle will adjust its vertical position and finally reach a steady state. This process can be captured by our two-phase LBM-DEM coupling model, and the contact angle is calculated by

$$\alpha = \arccos(h/R), \tag{24}$$

where  $h$  is the distance between the interface and the particle center, and  $R$  is the radius of the particle. Fig. 3c shows the comparison of the contact angles calculated by these two methods. For a given

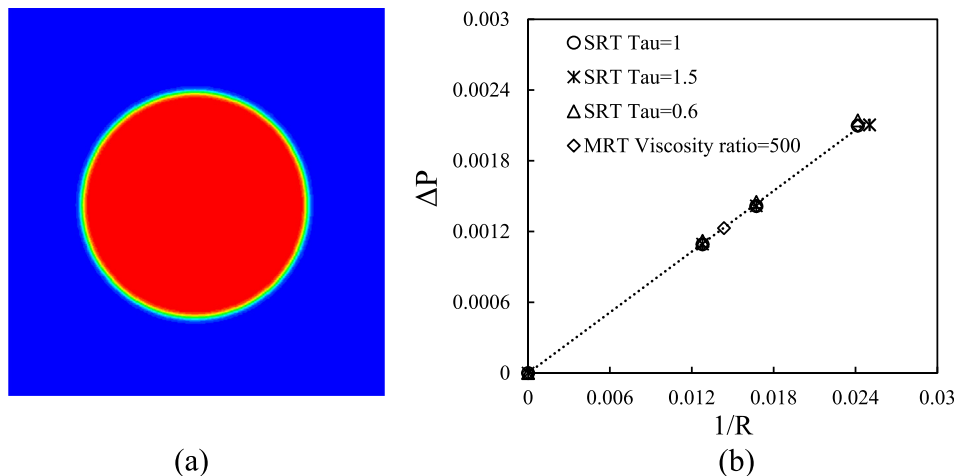
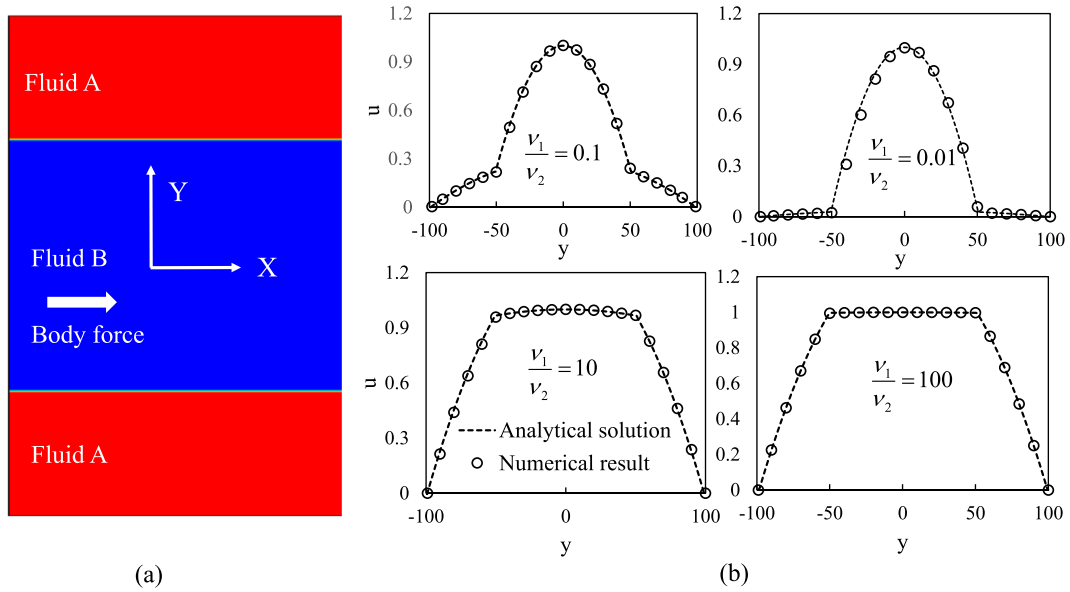


Fig. 1. Benchmark for a static bubble suspended in a fluid. (a) The computational domain is a square, and the diameter of the bubble varies from 41 to 78. (b) The linear fitting curve of results from SRT and MRT schemes, which follows the Laplace's law very well. The slope of the line corresponds to the surface tension. Compared with the original Shan-Chen model with SRT, the current MRT scheme can handle a high viscosity ratio up to 500.



**Fig. 2.** (a) Physical model of the co-current flow for the layered fluids with the different viscosity ratios (0.01, 0.1, 10 and 100). No-slip boundaries at top and bottom walls and periodic boundaries for inlet and outlet. A constant body force is applied in both fluids to drive the flow. (b) Comparisons between the numerical results and the analytical solutions for the velocity profiles, where the velocity is normalized by the maximum one for each case. The good agreements verify that the current model can successfully and accurately handle two-phase fluid flow with a high viscosity ratio.

**Table 2**  
LBM parameters in the second benchmark.

Group 1	$\nu_{red} = 0.00667, \nu_{blue} = 0.0667$	$\tau_{red} = 0.52, \tau_{blue} = 0.7$
Group 2	$\nu_{red} = 0.00667, \nu_{blue} = 0.667$	$\tau_{red} = 0.52, \tau_{blue} = 2.5$
Group 3	$\nu_{red} = 0.0667, \nu_{blue} = 0.00667$	$\tau_{red} = 0.7, \tau_{blue} = 0.52$
Group 4	$\nu_{red} = 0.667, \nu_{blue} = 0.00667$	$\tau_{red} = 2.5, \tau_{blue} = 0.52$

two-phase fluid-solid system (with the same interface parameters), the contact angles calculated by these two methods are very close to each other, which shows the correctness of the current two-

phase LBM-DEM coupling model in calculating the capillary force at the three-phase contact point.

### 3. Results and discussion

In this section, a rigid planar 2D sphere crossing a deformable fluid-fluid interface is simulated, and the whole process can be separated into two stages: before the particle contacts with the interface (see Fig. 4(a)) and after the particle contacts with the interface (see Fig. 4(b)). Therefore, the following discussion is arranged into two parts, “interfacial settling mode” and “tail dynamics”.

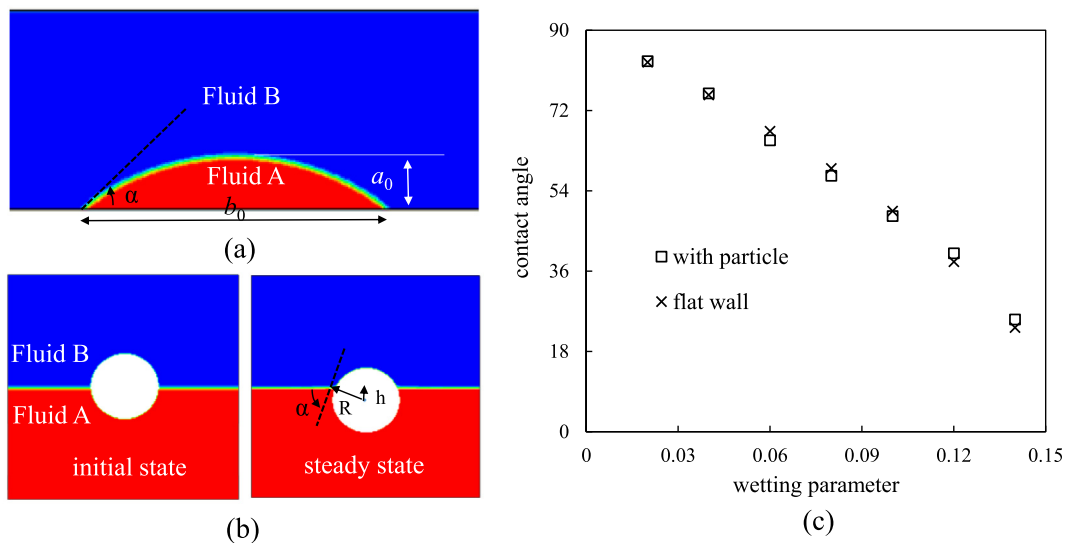


**Fig. 3.** Two methods for calculating the contact angle in a two-phase fluid solid system. (a) Sitting-drop scheme, where a droplet of fluid A is attached on a fixed solid wall. When the steady state is obtained, the contact angle can be calculated. (b) Suspending-particle scheme, where a solid spherical particle is initially placed at the interface between two phase fluids and released to adjust its vertical position owing to the capillary force to achieve a steady state. (c) Comparisons of the calculated contact angles by the two methods. The square symbols represent the ones calculated by the suspending-particle scheme and the cross symbols are calculated by the sitting-drop scheme. The results are consistent, which validate the accuracy and effectiveness of the current two-phase LBM-DEM coupling model for calculating the capillary force.

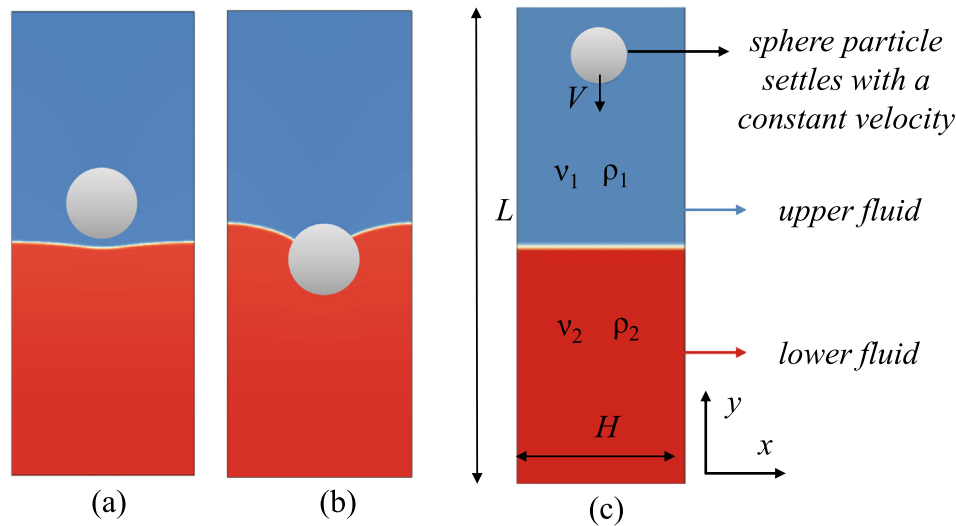


**Fig. 4.** Diagram showing the two stages during the particle motion passing through the fluid-fluid interface. (a) The first stage: before the particle contacts with the interface. (b) The second stage: after the particle contacts with the interface. (c) Computational domain is a closed channel, where the left and right boundaries are periodic and the fluid at the top and bottom boundaries is static. Binary immiscible fluids are separated by a deformable interface, and a rigid sphere moves down with the constant velocity.

The computational domain is shown in Fig. 4(c) with a  $300 \times 600$  grid/lattice. Periodic boundary conditions are applied on the left and right sides. Fluids on the top and bottom sides are static. Two fluids (red and blue) with the same density but different viscosities occupy the upper and lower parts respectively. Four cases with different viscosity ratios of the binary fluids (0.1, 1, 10, 100) are considered. In lattice unit, a rigid sphere ( $R = 45$ ) is released from the starting position (150,525), and settles down with the constant velocity, which varies from 0.001 to 0.03 (normalized by  $\delta_x/\delta_t$ ) in our simulations. The dimensionless parameters in this process are summarized in Table 3.

In order to validate the effectiveness of the current method in simulating the particle motion in binary immiscible fluids, two common transport modes (film drainage and tailing mode) (De Folter et al., 2010; Geller et al., 1986) are reproduced first. Fig. 5 shows the transport process of film drainage, where the viscosity ratio ( $\lambda$ ) and the particle Reynolds number ( $Re = VR/v_1$ ) equal to 10 and 2.7, respectively. As reported in the early experiments (De Folter et al., 2010), the passage of the particle by film drainage can be divided majorly into three stages: approach to the interface, passage through the interface and movement away from the interface. When the particle is away from the interface, the deformation of the latter is negligible just like a plate wall, as shown in Fig. 5a. As the particle approaches the interface, a film is formed between them and drained gradually, which is termed as “film drainage”. When the film drainage process is completely over, the particle connects with the interface and breaks through it, as shown in Fig. 5d. With the continuous movement of the particle away from the interface, a volume of the upper fluid is entrained into the

lower one and eventually pinches off just above the particle surface, as shown in Fig. 5e-g. These results are quite consistent with those from the experiments (De Folter et al., 2010) and other simulations (Geller et al., 1986).

Simulation results of tailing mode are presented in Fig. 6. The computational domain is a little bit longer with a  $300 \times 900$  grid/lattice. The simulation parameters are  $\lambda = 100$  and  $Re = 0.67$ . In tailing mode, the interface has remarkably deformed even when the particle is still away from it, as shown in Fig. 6a. A tail (column of the upper fluid) is entrained into the lower one even if the film has not been passed through, whose length is several times of the particle radius, as shown in Fig. 6b-e. Eventually, the tail pinches off at its middle part, as shown in Fig. 6f. The upper part moves towards the interface and the lower one is attached to the sphere surface, as shown in Fig. 6g. The simulated process is consistent with the experimental observations (Dietrich et al., 2011; Pierson and Magnaudet, 2018a) as shown in Fig. 6i (Dietrich et al., 2011).

### 3.1. Interfacial settling modes

This section focuses on the interface deformation mode before the particle contacts with the interface. We are trying to figure out the key dimensionless parameters governing the transition from film drainage to tailing mode. First, the Reynolds number ( $Re$ ) effect is checked and then the influence from Capillary number ( $Ca$ ) and viscosity ratio ( $\lambda$ ) is discussed.

#### 3.1.1. Reynolds number effects

In this process the spherical particle moves initially with a constant velocity in the fluid environment, and therefore the Reynolds number ( $Re$ ) has been naturally selected to characterize the particle movement (Magnaudet and Mercier, 2020). For the particle inertial settling under gravity only, since the stable settling velocity of particle before contacting with the interface depends on the gravity ( $g$ ), the Archimedes number ( $Ar$ ) is frequently used instead of the Reynolds number (Pierson and Magnaudet, 2018a, 2018b). In this sense,  $Re$  is more general than  $Ar$ , as the origin of particle velocity, stable settling or not, is not concerned. Thus, let us revisit  $Re$  as the critical characteristic dimensionless parameter for the interfacial settling mode.  $Re$ , defined as  $VR/v$ , is calculated by the settling velocity ( $V$ ) no matter if it is stable or not, the particle radius ( $R$ ) and the kinematic viscosity of fluid ( $v$ ) which is usually

**Table 3**  
Dimensionless parameters involved in the interface deformation.

Dimensionless parameter	Definition	Illustration
Reynolds number ( $Re$ )	$Re = RV/v_1$	Particle velocity $V$ ; Particle radius $R$ ; Upper fluid kinematic viscosity $v_1$
Capillary number ( $Ca$ )	$Ca = \mu_1 V/\sigma$	Particle velocity $V$ ; Upper fluid dynamic viscosity $\mu_1$ ; Surface tension $\sigma$
Viscosity ratio ( $\lambda$ )	$\lambda = \mu_1/\mu_2$	Upper fluid viscosity $\mu_1$ ; Lower fluid viscosity $\mu_2$
Normalized radius ( $r$ )	$r = R/H$	Particle radius $R$ ; channel width $H$

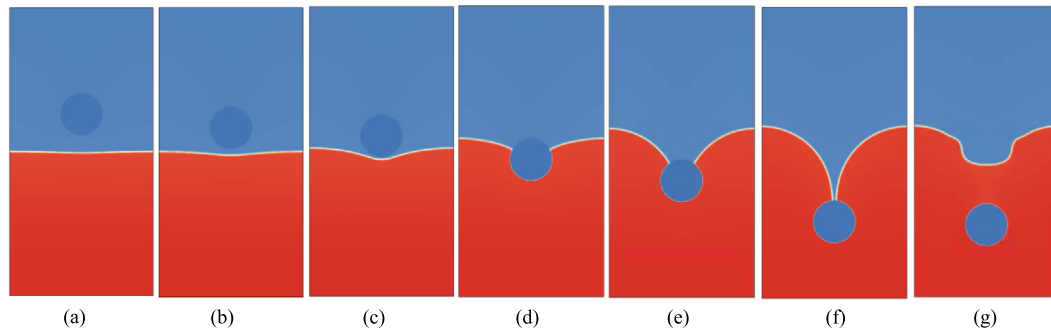


**Fig. 5.** Simulation results for a particle movement passing through a fluid-fluid interface by the film drainage mode. When the particle is away from the interface, the interface deformation is negligible (see (a)). With the particle approaching the interface, the film between the sphere and the interface is gradually drained, as termed as “film drainage” (see (b) and (c)). With the continuous motion of the particle away from the interface, a volume of upper fluid is entrained into the lower one and finally pinches off from the particle surface.

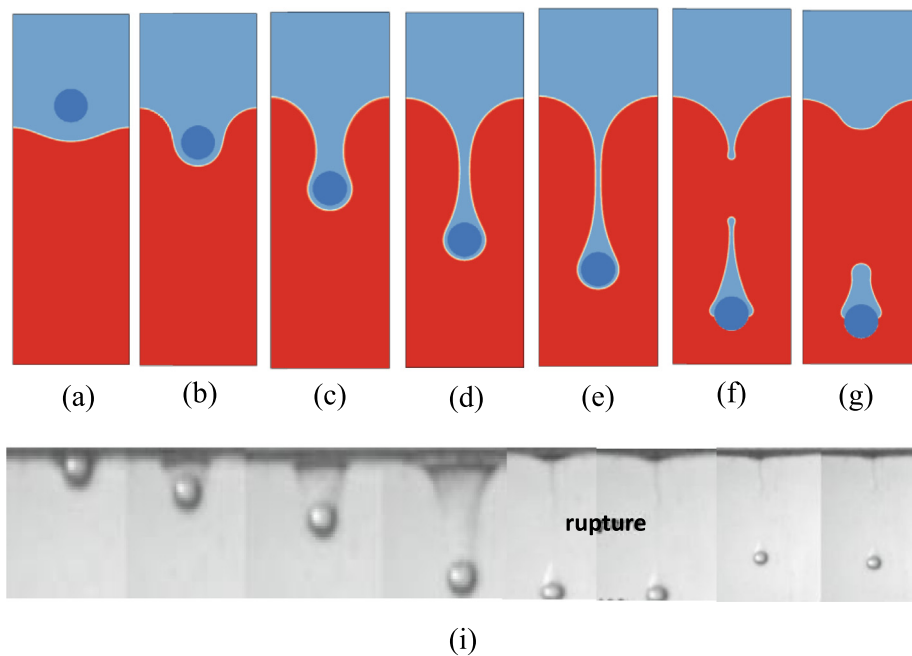


**Fig. 6.** Numerical results for the tailing mode transport process, where the interface remarkably deforms before the particle contacts with it (See a). A column of the upper fluid is entrained into the lower one even though the film drainage has not been completely over, whose length is several times of the particle radius (See b-e). Eventually, the column pinches off at its middle part. The upper part moves towards the interface, and the lower one is attached on the rear part of the particle. This process is very consistent with what is observed in the experiments (Dietrich et al., 2011) (See i).

the initial fluid. It is clear that a lower  $Re$  may come from different factors, lower velocity, smaller particles or higher viscosity of fluid. We will check the consistency of  $Re$  effects on the transport modes as follows.

#### A. $Re$ variation caused by fluid viscosity

Three cases are simulated here with the given lower fluid viscosity ( $\nu_2 = 0.00667$ ), the settling velocity ( $V = 0.007$ ) and the particle radius ( $R = 45$ ), and three different upper fluid viscosities ( $\nu_1 = 0.00667, 0.0667$  and  $0.667$ ) are considered to achieve various Reynolds number ( $Re = 0.47, 4.73$  and  $47.25$ ). To show the interfacial settling mode, two snapshots during the transport process are selected from each case as shown in Fig. 7. When the particle Reynolds number is high ( $Re = 47.25$ ), the interface deformation is negligible and the film drainage mode happens (see Fig. 7a). With the decrease of the particle Reynolds number, the interface begins to deform (see Fig. 7b). When  $Re$  is sufficiently small, tailing mode

is observed and the interface has significantly deformed before the particle connects with it (see Fig. 7c). Thus, it indicates that a smaller Reynolds number corresponds to a larger interface deformation, resulting in the transition of the transport mode from film drainage to tailing mode.

#### B. $Re$ variation caused by settling velocity and particle radius

On the other hand, a smaller Reynolds number may come from a lower particle velocity ( $V$ ) or a smaller particle size ( $R$ ). We consider both factors here. First the particle settling velocity varies from 0.004, 0.007, 0.01 to 0.03, which corresponds to  $Re = 2.7, 4.725, 6.75$  and  $20.25$  respectively, for given fluid viscosity ( $\nu_1 = 0.0667, \nu_2 = 0.00667$ ) and fixed particle radius ( $R = 45$ ). Fig. 8 shows when  $Re$  is small (small  $V$ ), the sphere crosses the interface with the film drainage mode (see 8a). As  $Re$  increases, the transport mode transforms from film drainage to tailing mode, which means that tailing mode prefers to happen for a higher  $Re$ .

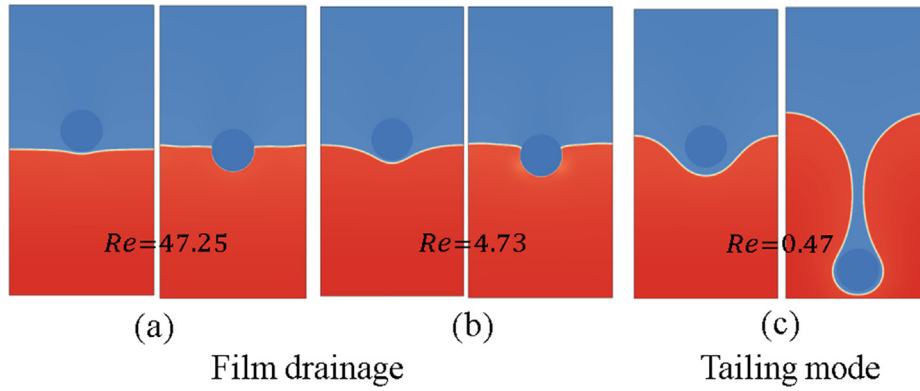


**Fig. 7.** Numerical results for different Reynolds number ( $Re$ ) caused by variation of the upper fluid viscosity. The lower fluid viscosity ( $\nu_2 = 0.00667$ ), the particle radius ( $R = 45$ ) and the settling velocity ( $V = 0.007$ ) are given. The difference comes from the upper fluid viscosity ( $\nu_1 = 0.00667, 0.0667$  and  $0.667$  corresponding to  $Re = 0.47, 4.73$  and  $47.25$ , respectively). For each  $Re$  two snapshots are selected to show the transport configurations, and the right one is the snapshot just before the particle connects with the interface (which means the particle has no contacted with the interface yet, but will contact at the next time step). As  $Re$  decreases, the transition of the transport mode from film drainage to tailing mode happens.

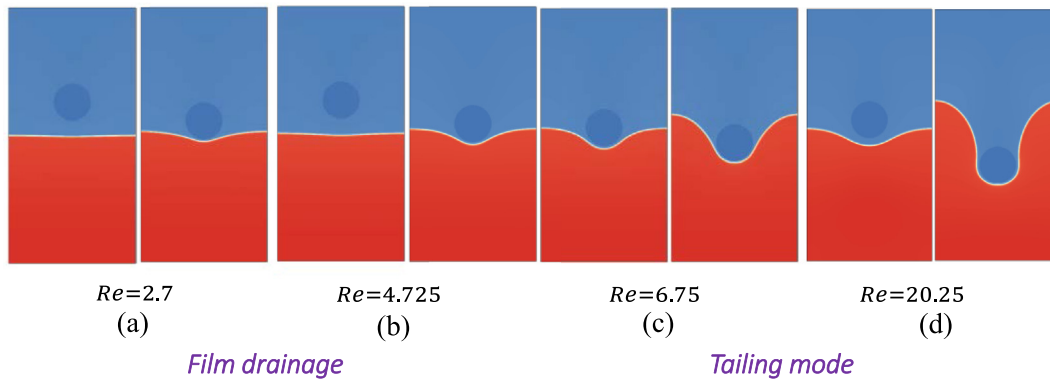


**Fig. 8.** Numerical results for different Reynolds number ( $Re$ ) cases caused by the variation of the settling velocity. In (a), (b), (c) and (d) the fluid viscosity ( $\nu_1 = 0.0667, \nu_2 = 0.00667$ ) and the particle radius ( $R = 45$ ) are same, and the unique difference is the settling velocity ( $V = 0.004, 0.007, 0.01$  and  $0.03$  corresponding to  $Re = 2.7, 4.725, 6.75$  and  $20.25$ , respectively). For each case two snapshots are selected to show the transport configurations, and the right one is the snapshot just before the particle connects with the interface. With the increase of Reynolds number, the transport mode transforms from film drainage to tailing mode.

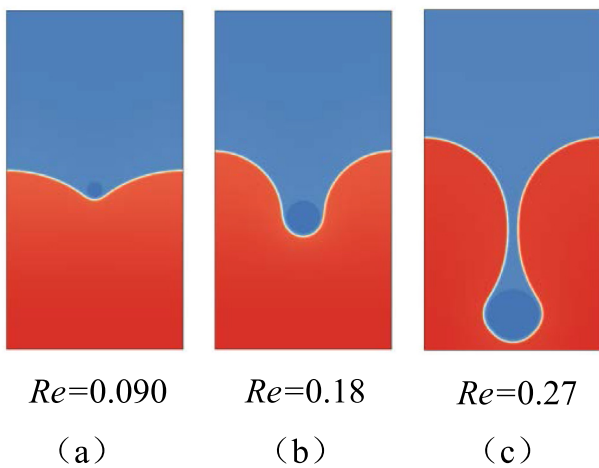


**Fig. 9.** Numerical results for different  $Re$  by changing particle radius ( $R$ ). The fluid viscosity ( $\nu_1 = 0.667, \nu_2 = 0.00667$ ) and the velocity ( $V = 0.004$ ) are given. The particle radius varies ( $R = 15, 30$  and  $45$  corresponding to  $Re = 0.09, 0.18$  and  $0.27$ , respectively). The snapshot is just before the particle connects with the interface to show the transport mode. As  $Re$  increases, the transport mode transforms from film drainage to tailing mode.

Next, the particle radius ( $R$ ) is changed for different  $Re$ . We consider three different value of  $R$  for a given particle velocity ( $V = 0.004$ ). According to Fig. 9, the tailing mode takes place when  $R$ , hence  $Re$ , increases, which is consistent with Fig. 8, but conflicts with Fig. 7. To summarize, the Reynolds number is not a proper dimensionless parameter to characterize the transport modes.

### 3.1.2. Regime maps based on Capillary number ( $Ca$ ) and viscosity ratio ( $\lambda$ )

In order to figure out the proper dimensionless parameters for the transport mode characterization, force analysis on the interface is necessary. The viscous force caused by the particle motion in the fluid is the driving force for the interface deformation, whose magnitude is proportional to the fluid viscosity ( $\nu$ ) and the particle velocity ( $V$ ). The resistance force for the interface deformation is caused by the surface tension ( $\sigma$ ) between the two immiscible fluids, which is calculated by the Laplace's Law (Eq. (21)). Thus, the Capillary number ( $Ca$ ), representing the relative effect of the viscous drag force versus the surface tension force

$$Ca = \frac{\rho \nu V}{\sigma}, \quad (25)$$

is chosen as one of the key parameters to characterize the interfacial settling mode. Usually the upper fluid properties ( $\rho_1, \nu_1$ ) are used to calculate the characteristic  $Ca$ . The interface deformation is governed by both fluids of the interface. Probably major influence comes from the upper fluid at the early stage, from both fluids during the transition stage and from the lower fluid at the late stage. If the interfacial deformation is remarkable, the entire process is governed by both fluids' properties. Therefore, we believe that the other key parameter, besides  $Ca$ , is the Capillary ratio between two fluids,

$$\lambda = \frac{Ca_1}{Ca_2} = \frac{\mu_1}{\mu_2}, \quad (26)$$

which is actually the viscosity ratio of two fluids. After the force analysis, the Capillary number together with viscosity ratio ( $Ca, \lambda$ ) are presented to characterize the particle movement passing through the deformable fluid-fluid interface.

This is not the first time to propose the Capillary number to characterize the particle motion through a deformable interface. Geller et al. (1986) used  $Ca$  to distinguish the film drainage mode and tailing mode, and they found tailing mode more easily occurred for large  $Ca$ . Yet, their studies focused only on the creeping flow (very small  $Re$ ) and early stage before pinch-off due to the limitation of the numerical method they used. By developing a new two-phase LBM-DEM coupling model, this work is able to study the entire process for a large range of parameters values, and to provide a regime map based on ( $Ca, \lambda$ ).

To give a comprehensive analysis, more cases with different Capillary numbers ( $Ca$ ) and different viscosity ratio ( $\lambda$ ) between upper and lower fluid have been considered. The viscosity ratio  $\lambda$  varies by three orders of magnitude (0.1, 1.0, 10 and 100) and the particle velocity varies from 0.001 to 0.03. Fig. 10 shows the snapshot just before particle contacts with interface for each case to demonstrate the interface deformation mode.

In order to distinguish the film drainage and the tailing mode quantitatively, a dimensionless tailing index ( $q$ ) is proposed in this work, as shown in Fig. 11, which is defined by the ratio of the largest tail length ( $L$ ) before the particle connects with the interface to the particle diameter ( $d = 2R$ )

$$q = \frac{L}{d}. \quad (27)$$

If  $q$  is much smaller than 1, the interface deformation is negligible and the film drainage happens. When  $q$  is much larger than 1, the interface deforms remarkably and the tailing mode happens.

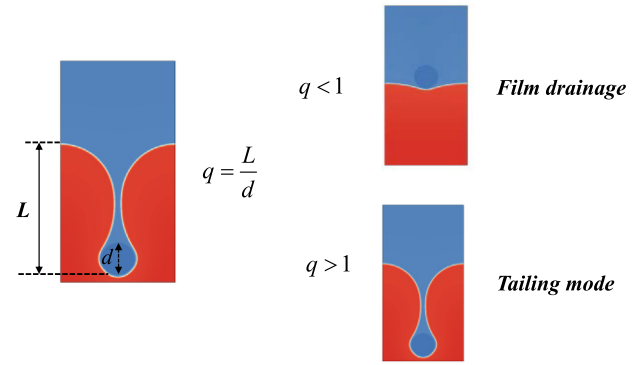


Fig. 11. Diagram used to illustrate the calculation of index  $q$ , which is defined by the ratio of the largest tail length ( $L$ ) before the particle connects with the interface to the particle diameter ( $d$ ). When index  $q$  is much smaller than 1, the interface deformation is negligible and film drainage happens. When index  $q$  is much larger than 1, the interface is greatly deformed and tailing mode happens.

Numerical results in Fig. 10 are summarized in Fig. 12. Fig. 12a is a regime map showing the index  $q$  distribution in the ( $\lambda, Ca$ ) diagram. The red and blue region corresponds to the tailing mode and the film drainage mode, respectively. All the film drainage mode falls in the smaller Capillary number region and the tailing mode more easily happens at the larger Capillary number region. For cases with the same viscosity ratio, a critical Capillary number exists, above which the transition from film drainage to tailing mode happens. In addition, this critical  $Ca$  is nearly independent of the viscosity ratio ( $\lambda$ ). Fig. 12b shows the index  $q$  under different Capillary number, where two regions are divided according to the interfacial settling mode. The critical Capillary number for the transition from film drainage to tailing mode is around 0.01. Current simulations quantitatively show that tailing mode more easily happens at larger  $Ca$ . These results prove again that,  $Ca$ , rather than  $Re$ , is the key dimensionless parameter governing the transport configurations.

The discussion above is based on a fixed particle size ( $R = 45$ ), and in order to show the size effects on the interface deformation mode, particles with different radius are considered ( $R = 15$  and  $30$ ). For each particle size, four cases with different Capillary number are simulated, and the parameters are listed in Table 4. Simulation results are summarized in Fig. 13, where the particle size is normalized as Reynold number ( $Re$ ), which shows that the critical

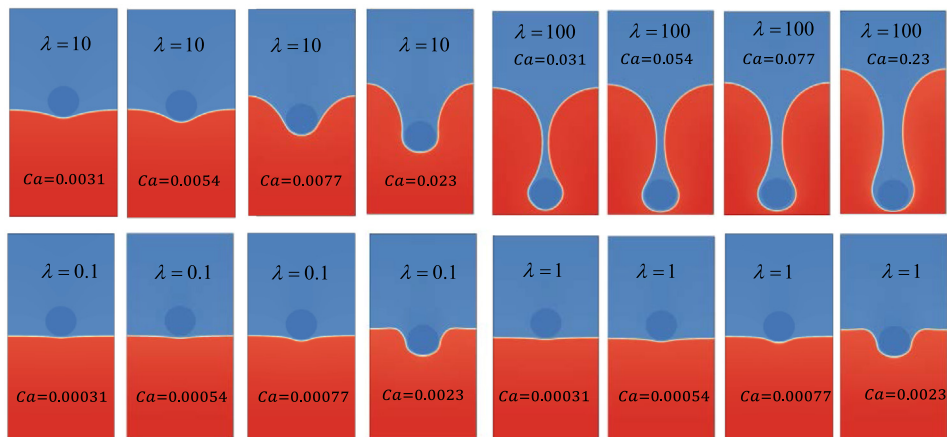
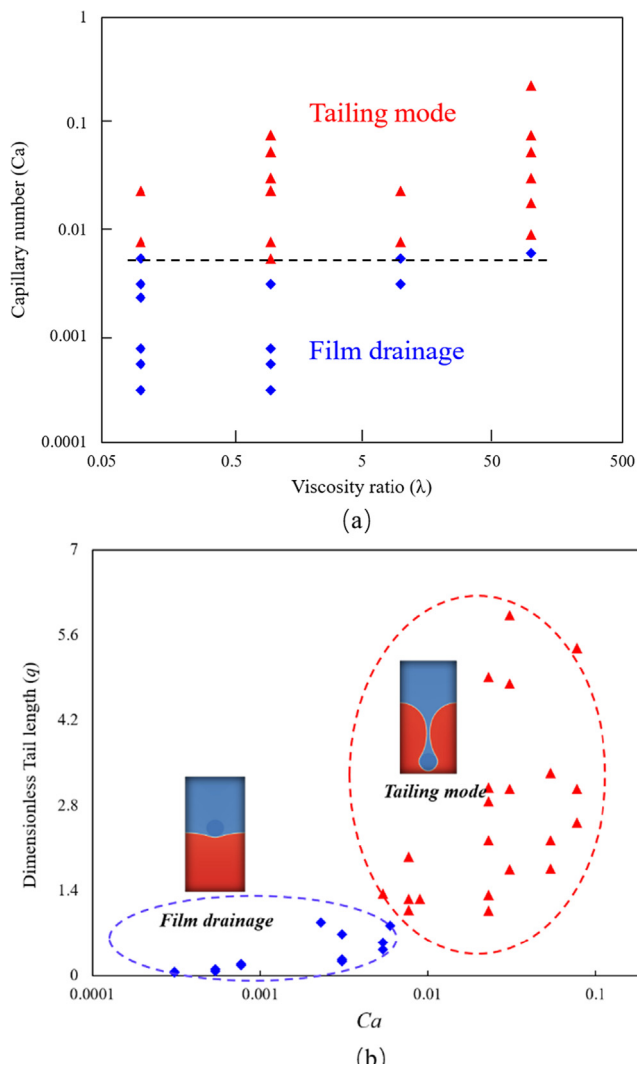


Fig. 10. Simulation results for more cases with different Capillary numbers ( $Ca$ ) where the kinematic viscosity ratio ( $\lambda$ ) between the upper and lower fluid varies by three orders of magnitude (0.1, 1.0, 10 and 100), and the particle settling velocity varies from 0.001 to 0.03. The smaller value of the fluid viscosity in each case is equal to 0.0067 and the surface tension ( $\sigma$ ) equals to 0.0865. For each case the snapshot just before the particle contacts with interface is given to show the transport configuration.



**Fig. 12.** (a) Regime map of  $Ca-\lambda$  showing the distribution of film drainage and tailing mode by which the particle passes through the fluid-fluid interface. The red region means high index  $q$  corresponding to tailing mode, and the blue region means low index  $q$  corresponding to the film drainage mode. Film drainage falls in the low  $Ca$  region, and tailing mode more easily happens at large  $Ca$  situations. (b) Variation of index  $q$  under different Capillary number, where two regions are divided, and the critical  $Ca$  for the transition from film drainage to tailing mode is around 0.01. (For interpretation of the references to colour in this figure legend, the reader is referred to the web version of this article.)

**Table 4**  
LBM parameters for each particle size.

Case 1	$v_{red} = 0.00667, v_{blue} = 0.0667$	$V = 0.03 \sigma = 0.0865$
Case 2	$v_{red} = 0.00667, v_{blue} = 0.667$	$V = 0.004 \sigma = 0.0865$
Case 3	$v_{red} = 0.00667, v_{blue} = 0.667$	$V = 0.007 \sigma = 0.0865$
Case 4	$v_{red} = 0.00667, v_{blue} = 0.667$	$V = 0.01 \sigma = 0.0865$

$Ca$  allowing the particle to pass the interface by tailing mode is nearly independent of the Reynolds number ( $Re$ ). It is consistent with the result in Section 3.1.1 that Reynolds number is not a proper dimensionless parameter to characterize the transport modes.

The main objective of this work is to figure out the key dimensionless number governing the interfacial settling mode. Using the current new model, tailing mode and film drainage are successfully

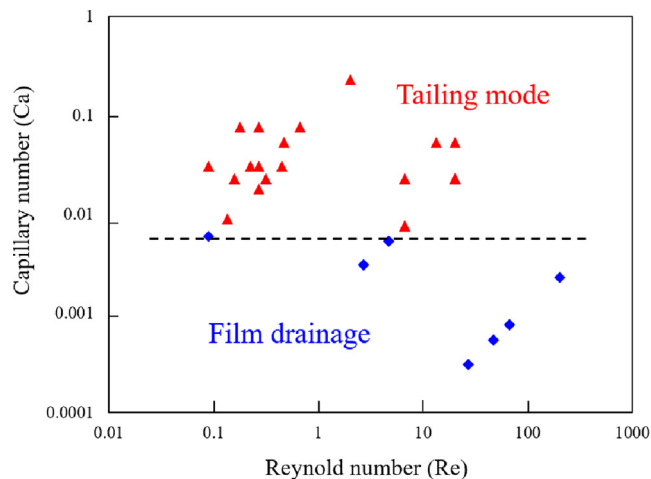


**Fig. 13.** (a) Regime map  $Ca-Re$  shows the distribution of film drainage and tailing mode by which the particle passes through the fluid-fluid interface. Three particle sizes are considered, which are normalized as Reynolds number ( $Re$ ), and the results in Fig. 10 are also summarized. Tailing mode is promoted in the high Capillary number region. Film drainage falls in the low Capillary number region.

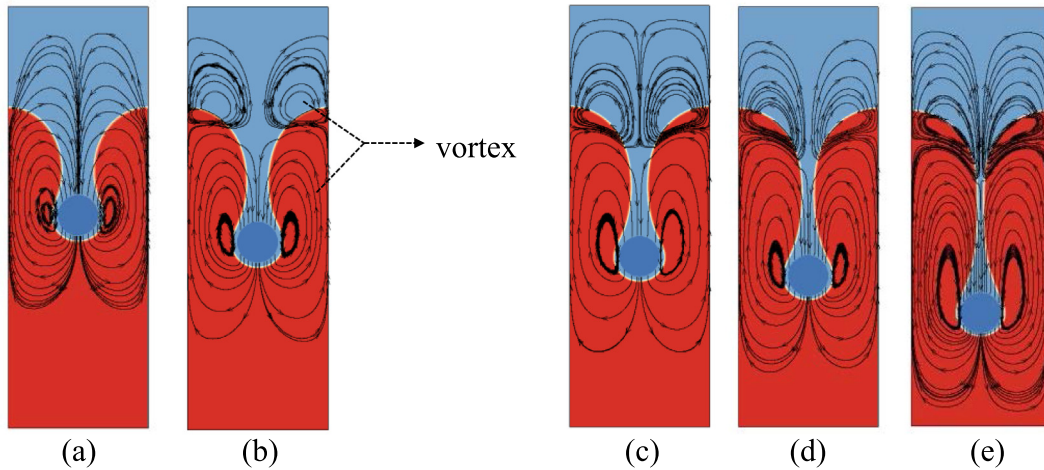
reproduced as presented in Fig. 6, which is consistent with the experimental observation. The current model is in 2D, however, a 3D model will be developed in the future and providing more direct comparison with the experiments.

### 3.2. Tail dynamics

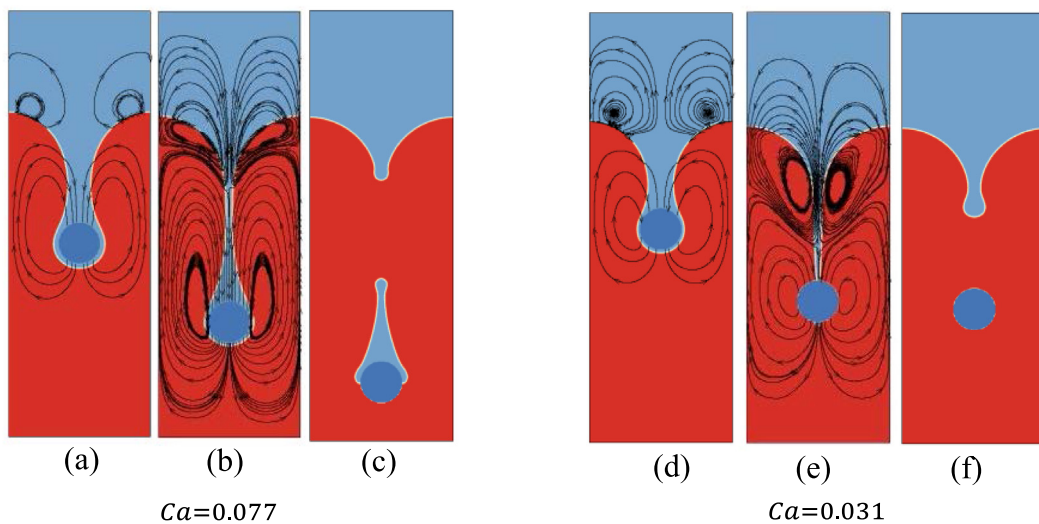
Tail dynamics means the fluid dynamics in the tail region which is important to understand the late behavior of tail, including the final tail length and its pinch-off position (Dietrich et al., 2011; Pierson and Magnaudet, 2018a). In this section, the tail dynamics for the tailing mode transport process is explored.

Fig. 14 shows the typical snapshots of streaming lines of fluid velocity for the tailing mode. At the early stage of tailing mode, the fluid velocity in the tail is always downward just as that of particle motion in the single-phase fluid, and one vortex exists on each side of the sphere as shown in Fig. 14a. With the increase of liquid volume, the upward flow in the upper region of tail is observed as shown in Fig. 14b, which is caused by the interface covering-up. A point with zero velocity (instantaneous points) exists to separate these two opposite flows as shown in Fig. 14b. Two vortices are formed on each side of the instantaneous point, which stretch the tail in two opposite directions. As a result, the rupture happens in the middle part of the liquid column as shown in Fig. 14e. Upward flow near the interface is also observed in experiments (Dietrich et al., 2011) and other numerical results (Camassa et al., 2010; Manga and Stone, 1995). With the increase of the tail length, the instantaneous point separating the upward and downward flow moves gradually towards the lower part of tail as shown in Fig. 14c-e. Fig. 14e shows the snapshot just before the rupture of tail happens, which illustrates that the rupture position is near the instantaneous point for the thinnest tail.

Based on the current simulations, we find that the existence of upward flow affects the final tail length and its pinch-off position. Fig. 15 shows the tail dynamics for  $Ca = 0.031$  and  $0.077$ . In each case, three snapshots are selected. The left ones (Fig. 15a and d) are the snapshots when the upward flow is first observed. The middle ones (Fig. 15b and e) are the snapshots just before rupture of the tail happens. The right ones (Fig. 15c, 15f) are the snapshots just after the tail pinches off. When Capillary number is relatively small ( $Ca = 0.031$ ), the upward flow is observed when the tail



**Fig. 14.** Snapshots for the particle passing through the fluid-fluid interface. Initially, the fluid velocity is downwards just as the particle settles in the single-phase fluid (see a). Then the upward flow is observed in the upper region of the tail, and a transition point exists to separate the two-opposite flow (see b). With the increase of the tail length, this transition point moves gradually towards the lower part of tail. Finally, the tail pinches off near the transition point owing to the stretching caused by the upper and lower vortex on each side of the transition point.



**Fig. 15.** Snapshots for tail dynamics in  $Ca = 0.031$  and  $0.077$  cases. In each case, three snapshots are selected. The left one ((a), (d)) is the snapshot when the upward flow is first observed. The middle one ((b), (e)) is the snapshot just before the tail rupture happens. The right one ((c), (f)) is the snapshot just after the tail pinches off.

length is short ( $6.15 R$ ), and the instantaneous point separating the upward and downwards flow is close to the particle. As a result, the final tail length before it pinches off is short ( $9.14 R$ ) and the rupture position is close to the particle. If  $Ca$  increases ( $Ca = 0.077$ ), the upward flow happens when the tail length is relatively long ( $7.02 R$ ), leading to a long final tail length ( $12.96 R$ ). The rupture position is at the middle part of the tail, and a droplet is attached on the rear part of the particle.

For a quantitative exploration of the Capillary number effects on the tail dynamics, a dimensionless tail length ( $l_u = l/R$ ) when the upward flow is first observed (solid line in Fig. 16a, termed as  $l_u$  in the following part) and final tail length ( $l_f = l/R$ ) before the rupture happens (dash line in Fig. 16a, termed as  $l_f$  in the following part) are plotted. When the particle passes through the interface with a smaller  $Ca$ , the upward flow is more easily formed at the shorter tail length ( $l_u$ ), which results in the shorter final tail length ( $l_f$ ) entrained by the particle motion. This conclusion is

further illustrated by Fig. 16b, which shows the relationship between  $l_u$  and  $l_f$ .

#### 4. Conclusions

In this paper, we performed a series of numerical simulations aiming at characterizing various transport modes for the particle motion passing through a deformable fluid-fluid interface. A two-phase LBM-DEM coupling model was developed in this work to simulate the particle motion in a two-phase fluid system, which overcomes the limitation of the previous models in dealing with fluid-fluid-solid system with the high viscosity ratio. After validations, the model is used to study a single spherical particle movement passing through the fluid-fluid interface. Two important transport modes, film drainage and tailing mode, are successfully reproduced. The underlying phy-

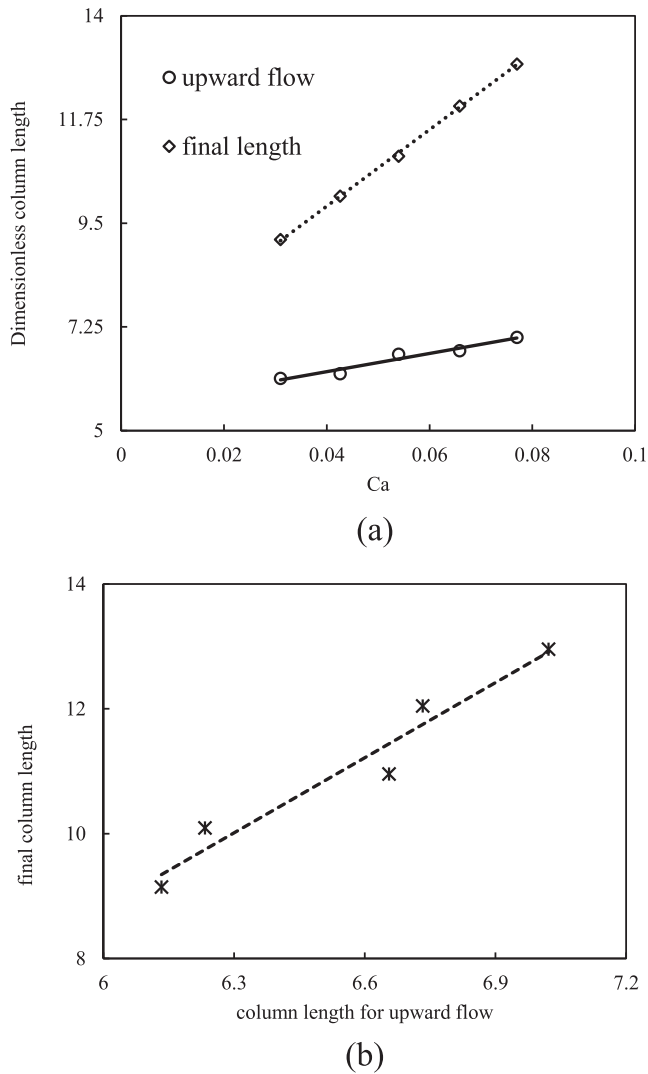


**Fig. 16.** Diagram showing the tail dynamics effects on the final tail length. (a) Variation of dimensionless tail length for the first appearance of the upward flow and the final tail length before the pinch-off in different Capillary number cases. (b) Relationship between the tail length for the first appearance of the upward flow and the final tail length before the pinch-off.

sics governing the interfacial settling mode is systematically explored, and the following conclusions can be drawn.

- (i) For the particle movement through a fluid-fluid interface with comparable fluid densities, Capillary number rather than Reynolds number is a proper dimensionless parameter governing the interfacial settling mode. In this work, a regime map is given to show the distribution of film drainage and tailing mode in  $(\lambda, Ca)$  diagram. Film drainage falls in the small Capillary number ( $Ca$ ) region and tailing mode more easily happens at large Capillary number ( $Ca$ ) situations. For each viscosity ratio, a critical Capillary number exists, above which the transition from film drainage to tailing mode happens. This critical  $Ca$  for a particle passing through the interface by tailing mode is nearly independent of the viscosity ratio but increases with the reduction of particle size.
- (ii) Tail dynamics affects significantly the tail pinch-off position and its final length. In the tailing mode, a tail of upper fluid is entrained into the lower one. When the tail length reaches a critical value, the upward flow in the upper region of the tail is observed, which is consistent with the experimental observations. We found that this critical tail length for the first

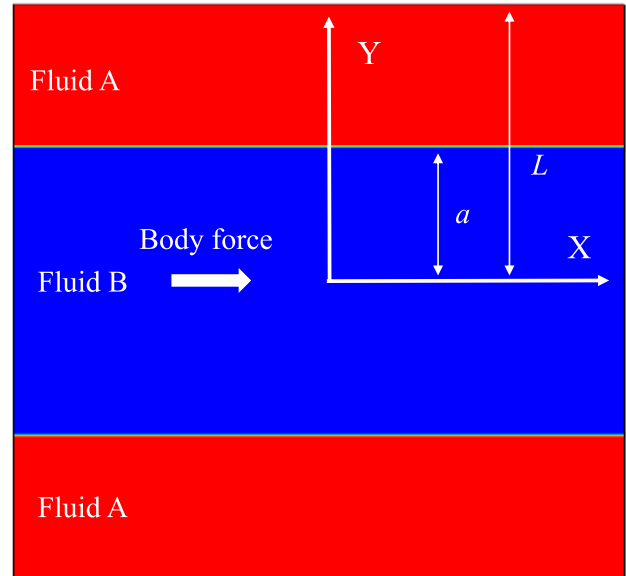


**Fig. A1.** Physical model of co-current flow for layered fluid, which includes two kinds of fluid (fluid A and fluid B) whose properties are same except kinematic viscosity. Fluid velocity is equal to zero at top and bottom boundaries and periodic boundaries are applied for left and right boundaries. A body force is applied in both fluid A and B to drive the whole system.

appearance of the upward flow influences the final tail length and its rupture position. When the particle passes through the interface with a smaller  $Ca$ , the upward flow is formed at the shorter tail length, which results in the shorter final tail length and the rupture position is closer to the particle surface.

#### CRediT authorship contribution statement

**Zhiqiang Chen:** Software, Formal analysis, Visualization, Writing - original draft. **Moran Wang:** Conceptualization, Writing - review & editing, Funding acquisition. **Shiyi Chen:** Conceptualization, Supervision.

#### Declaration of Competing Interest

We declare that there is no conflict of interests for this work.

#### Acknowledgements

This work is financially supported by the NSFC-DFG grant (No. 11761131012) and the National Key Research and Development Program of China (No. 2019YFA0708704).

#### Appendix A. The transformation matrix

In the current model, the multiple-relaxation-time (MRT) formulation is applied, and the transformation matrix  $T$  is given by Eq. (A1),

$$T = \frac{1}{36} \begin{bmatrix} 4 & 4 & 4 & 4 & 4 & 4 & 4 & 4 & 4 \\ -4 & -1 & 2 & -1 & 2 & -1 & 2 & -1 & 2 \\ 4 & -2 & 1 & -2 & 1 & -2 & 1 & -2 & 1 \\ 0 & 6 & 6 & 0 & -6 & -6 & -6 & 0 & 6 \\ 0 & -6 & 3 & 0 & -3 & 6 & -3 & 0 & 3 \\ 0 & 0 & 6 & 6 & 6 & 0 & -6 & -6 & -6 \\ 0 & 0 & 3 & -6 & 3 & 0 & -3 & 6 & -3 \\ 0 & 9 & 0 & -9 & 0 & 9 & 0 & -9 & 0 \\ 0 & 0 & 9 & 0 & -9 & 0 & 9 & 0 & -9 \end{bmatrix}. \quad (\text{A1})$$

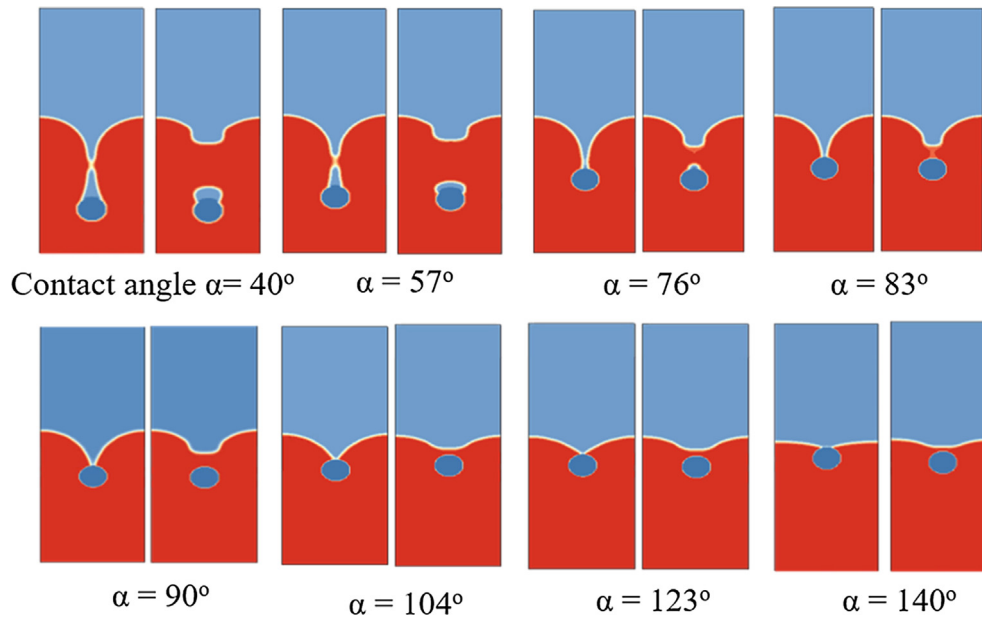


**Fig. A2.** Wetting property effect on the particle movement through a fluid-fluid interface. When the contact angle is small, a large volume of upper fluid is entrained into the lower one, and the rupture position is in the middle part of column. With the increase of the contact angle, the volume of the liquid entrained into the lower one decreases, and the rupture position becomes closer to the sphere surface.

## Appendix B. Layered co-current flow

Analytical solution for co-current flow is given in this part, and the computation domain is presented in Fig. A1 where the fluid A flows along the walls ( $a \leq |y| \leq L$ ) and the fluid B is between the fluid A ( $0 \leq |y| \leq a$ ). A body force  $F_b$  is applied on both fluid A and fluid B. For laminar flow, the analytical solution for the velocity profile in  $y$  direction of this system is

$$u(y) = \frac{F_b}{2\nu_B\rho_B}(a^2 - y^2) + \frac{F_b}{2\nu_A\rho_A}(L^2 - a^2), \quad 0 \leq |y| \leq a, \quad (\text{A2})$$

$$u(y) = \frac{F_b}{2\nu_A\rho_A}(L^2 - y^2), \quad a \leq |y| \leq L,$$

where the subscripts A and B refer to fluid A and B, respectively.

## Appendix C. Wetting property effect

The above discussions are based on the neutral-wetting situation (contact angle =  $90^\circ$ ). Here, different contact angles (contact angle  $40^\circ$ ,  $57^\circ$ ,  $76^\circ$ ,  $83^\circ$ ,  $90^\circ$ ,  $104^\circ$ ,  $123^\circ$ ,  $140^\circ$ ) are considered to explore the wetting property effect on the transport process preliminarily. Wetting properties only affect the process after the particle contacts with the interface (three contact point appearance). Thus, for each case two snapshots after the breakthrough of the interface are selected to illustrate the contact angle effects on the transport process. When the particle moves from wetting phase to non-wetting phase (contact angle =  $40^\circ$ ), a volume of upper fluid is entrained into the lower one and a small droplet is attached on the rear part of the sphere, as shown in Fig. A2. However, when it crosses the interface from non-wetting to wetting phase (contact angle =  $140^\circ$ ), nearly no upper fluid is entrained into the lower one and the interface deformation is negligible. Thus, contact angle has a great effect on the process after the particle crosses the interface, and the further exploration will be provided in our future work.

## References

- Aidun, C.K., Lu, Y.N., Ding, E.J., 1998. Direct analysis of particulate suspensions with inertia using the discrete Boltzmann equation. *J. Fluid Mech.* 373, 287–311.
- Ardekani, A.M., Doostmohammadi, A., Desai, N., 2017. Transport of particles, drops, and small organisms in density stratified fluids. *Phys. Rev. Fluids* 2, (10) 100503.
- Burns, P., Chemel, C., 2015. Interactions between downslope flows and a developing cold-air pool. *Bound.-Layer Meteor.* 154 (1), 57–80.
- Camassa, R., Falcon, C., Lin, J., McLaughlin, R.M., Mykins, N., 2010. A first-principle predictive theory for a sphere falling through sharply stratified fluid at low Reynolds number. *J. Fluid Mech.* 664, 436–465.
- Chen, Y., Kang, Q.J., Cai, Q.D., Wang, M.R., Zhang, D.X., 2015. Lattice boltzmann simulation of particle motion in binary immiscible fluids. *Commun. Comput. Phys.* 18 (3), 757–786.
- Chen, Z.Q., Wang, M.R., 2017. Pore-scale modeling of hydromechanical coupled mechanics in hydrofracturing process. *J. Geophys. Res. Solid Earth* 122 (5), 3410–3429.
- Chen, Z.Q., Xie, C.Y., Chen, Y., Wang, M.R., 2016. Bonding strength effects in hydro-mechanical coupling transport in granular porous media by pore-scale modeling. *Computation* 4 (1), 4010015.
- Chen, Z.Q., Yang, Z.M., Wang, M.R., 2018. Hydro-mechanical coupled mechanisms of hydraulic fracture propagation in rocks with cemented natural fractures. *J. Pet. Sci. Eng.* 163, 421–434.
- de Folter, J.W.J., de Villeneuve, V.W.A., Aarts, D., Lekkerkerker, H.N.W., 2010. Rigid sphere transport through a colloidal gas-liquid interface. *New J. Phys.* 12, 023013.
- Dietrich, N., Poncin, S., Li, H.Z., 2011. Dynamical deformation of a flat liquid-liquid interface. *Exp. Fluids* 50 (5), 1293–1303.
- Geller, A.S., Lee, S.H., Leal, L.G., 1986. The creeping motion of a spherical-particle normal to a deformable interface. *J. Fluid Mech.* 169, 27–69.
- Gunther, F., Janoschek, F., Frijters, S., Harting, J., 2013. Lattice Boltzmann simulations of anisotropic particles at liquid interfaces. *Comput. Fluids* 80, 184–189.
- Hartland, S., 1969. Profile of draining film between a rigid sphere and a deformable fluid-liquid interface. *Chem. Eng. Sci.* 24 (6), 987–995.
- He, X., Chen, S., Doolen, G.D., 1998. A novel thermal model for the lattice Boltzmann method in incompressible limit. *J. Comput. Phys.* 146 (1), 282–300.
- Jeffreys, G. V., and G. A. Davies (1971), In *Recent Advance in Liquid/Liquid Extraction*.
- Jones, A.F., Wilson, S.D.R., 1978. The film drainage problem in droplet coalescence. *J. Fluid Mech.* 87, 263–288.
- Kundakovic, L., Vunjak-Novakovic, G., 1995. Mechanics of particle motion in three-phase flow. *Chem. Eng. Sci.* 50 (20), 3285–3295.
- Ladd, A.J.C., 1994a. Numerical simulations of particulate suspensions via a discretized Boltzmann-equation. 1. Theoretical foundation. *J. Fluid Mech.* 271, 285–309.
- Ladd, A.J.C., 1994b. Numerical simulations of particulate suspensions via a discretized Boltzmann-equation. 2. Numerical results. *J. Fluid Mech.* 271, 311–339.

- Lee, H., Fouxon, I., Lee, C., 2019. Sedimentation of a small sphere in stratified fluid. *Phys. Rev. Fluids* 4, (10) 104101.
- Magnaudet, J., Mercier, M.J., 2020. Particles, Drops, and Bubbles Moving Across Sharp Interfaces and Stratified Layers. *Annual Review of Fluid Mechanics* 52, 61–91.
- Manga, M., Stone, H.A., 1995. Low-Reynolds-number motion of bubbles, drops and rigid spheres through fluid-fluid interfaces. *J. Fluid Mech.* 287, 279–298.
- Maru, H.C., Wasan, D.T., Kintner, R.C., 1971. Behavior of a rigid sphere at a liquid-liquid interface. *Chem. Eng. Sci.* 26 (10), 1615–1628.
- Milan, F., Biferale, L., Sbragaglia, M., Toschi, F., 2020. Lattice Boltzmann simulations of droplet breakup in confined and time-dependent flows. *Phys. Rev. Fluids* 5, (3) 033607.
- Panah, M., Blanchette, F., Khatiri, S., 2017. Simulations of a porous particle settling in a density-stratified ambient fluid. *Phys. Rev. Fluids* 2, (11) 114303.
- Pierson, J.L., Magnaudet, J., 2018a. Inertial settling of a sphere through an interface. Part 1. From sphere flotation to wake fragmentation. *J. Fluid Mech.* 835, 762–807.
- Pierson, J.L., Magnaudet, J., 2018b. Inertial settling of a sphere through an interface. Part 2. Sphere and tail dynamics. *J. Fluid Mech.* 835, 808–851.
- Porter, M.L., Coon, E.T., Kang, Q., Moulton, J.D., Carey, J.W., 2012. Multicomponent interparticle-potential lattice Boltzmann model for fluids with large viscosity ratios. *Phys. Rev. E* 86, (3) 036701.
- Princen, H.M., 1963. Shape of a fluid drop at a liquid-liquid interface. *J. Colloid Sci.* 18 (2), 178–195.
- Shah, S.T., Wasan, D.T., Kintner, R.C., 1972. Passage of a liquid drop through a liquid-liquid interface. *Chem. Eng. Sci.* 27 (5), 881–893.
- Shan, X.W., Chen, H.D., 1993. Lattice Boltzmann model for simulating flows with multiple phases and components. *Phys. Rev. E* 47 (3), 1815–1819.
- Shan, X.W., Chen, H.D., 1994. Simulation of nonideal gases and liquid-gas phase-transitions by the lattice Boltzmann-equation. *Phys. Rev. E* 49 (4), 2941–2948.
- Smith, P.G., Vandeven, T.G.M., 1984. The effect of gravity on the drainage of a thin liquid-film between a solid sphere and a liquid fluid interface. *J. Colloid Interface Sci.* 100 (2), 456–464.
- Song, F., Wang, W., Li, J., 2013. A lattice Boltzmann method for particle-fluid two-phase flow. *Chem. Eng. Sci.* 102, 442–450.
- Su, J., Chai, G., Wang, L., Cao, W., Gu, Z., Chen, C., Xu, X.Y., 2019. Pore-scale direct numerical simulation of particle transport in porous media. *Chem. Eng. Sci.* 199, 613–627.
- Sutherland, B.R., Gingras, M.K., Knudson, C., Steverango, L., Surma, C., 2018. Particle-bearing currents in uniform density and two-layer fluids. *Phys. Rev. Fluids* 3, (2) 023801.
- Truscott, T.T., Epps, B.P., Belden, J., 2014. Water Entry of Projectiles. *Annu. Rev. Fluid Mech.* 46 (1), 355–378.
- Tsai, S.S.H., Wexler, J.S., Wan, J., Stone, H.A., 2011. Conformal coating of particles in microchannels by magnetic forcing. *Appl. Phys. Lett.* 99, (15) 153509.
- Wei, B., Huang, H., Hou, J., Sukop, M.C., 2018. Study on the meniscus-induced motion of droplets and bubbles by a three-phase Lattice Boltzmann model. *Chem. Eng. Sci.* 176, 35–49.
- Xie, C.Y., Lei, W.H., Wang, M.R., 2018. Lattice Boltzmann model for three-phase viscoelastic fluid flow. *Phys. Rev. E* 97, (2) 023312.
- Xie, C.Y., Zhang, J.Y., Bertola, V., Wang, M.R., 2016. Lattice Boltzmann modeling for multiphase viscoplastic fluid flow. *J. Non-Newton. Fluid Mech.* 234, 118–128.
- Zhao, N., Wang, B., Kang, Q., Wang, J., 2020. Effects of settling particles on the bubble formation in a gas-liquid-solid flow system studied through a coupled numerical method. *Phys. Rev. Fluids* 5, (3) 033602.